A time projection chamber for the three-dimensional reconstruction of two-proton radioactivity events

B. Blank [a], L. Hay [a], J. Huikari [a], S. Leblanc [a], S. List [a], J.-L. Pedroza [a], P. Ascher [a], L. Audirac [a], C. Borcea [a,b], G. Canchel [a], F. Delalee [a], C.E. Demonchy [a], C. Dossat [a,c], J. Giovinazzo [a], P. Hellmuth [a], C. Marchand [a], I. Matea [a], R. de Oliveira [d], J. Pibernat [a], A. Rebii [a], L. Serani [a], J.C. Thomas [e]

[a] *Centre d'Etudes Nucléaires de Bordeaux Gradignan - Université Bordeaux 1 - UMR 5797 CNRS/IN2P3, Chemin du Solarium, BP 120, 33175 Gradignan Cedex, France*

[b] *NIPNE, P.O. Box MG6, Bucharest-Margurele, Romania*

[c] *DAPNIA, CEA Saclay, F-91191 Gif-sur-Yvette Cedex, France*

[d] *CERN, CH-1211 Geneva 23, Switzerland*

[e] *Grand Accélérateur National d'Ions Lourds, CEA/DSM - CNRS/IN2P3, Bvd Henri Becquerel, BP 55027, F-14076 CAEN Cedex 5, France*

Abstract

Two-proton radioactivity was observed in 2002 in the decay of ^{45}Fe. However, the experiments performed at that time did not allow the observation of the two protons directly. We present here a new setup based on the principle of a time-projection chamber which enabled us for the first time to identify directly the two protons. The new setup permits the observation and reconstruction in three dimensions of the traces of the protons and to determine thus their individual energies and their relative angle. We will discuss the setup in all necessary details and describe its performances in the context of two-proton radioactivity and β-delayed two-proton emission studies.

Key words: two-proton radioactivity, time projection chamber, ASIC electronics
PACS: 29.40.Cs, 29.30.Ep, 29.90.+r

1. Introduction

In 1960, Goldanskii [1] proposed two-proton radioactivity as a new radioactive decay mode to occur for nuclei for which the emission of one proton is energetically forbidden, but simultaneous two-proton emission from the ground state is allowed due to the nuclear pairing energy. Since then theoretical considerations [2–5] and experimental observations [6–8] allowed to determine ^{45}Fe, ^{48}Ni, ^{54}Zn and other nuclei in this mass region to be the most promising candidates for this new decay mode.

In experiments at the GANIL LISE3 separator [9] and at the FRS of GSI [10], ground-state two-proton (2p) emission was indeed observed for the first time in the decay of ^{45}Fe. However, although these experiments clearly established 2p radioactivity to be the only decay mode which could consistently explain all observational details [9,10], they did not allow the direct observation of the two protons emitted. This is linked to the fact that the decay of ^{45}Fe was observed in silicon detectors in which the ions of interest were deeply implanted. Therefore, only the total decay energy, the half-life, and the absence of β particles from the competing decay by β-delayed charged-particle emission could be firmly established. In addition, the observation of the daughter decay [11] helped to unambiguously assign the observed decay to 2p radioactivity.

This observation for ^{45}Fe as well as the study of the decay of ^{54}Zn[12] and possibly of ^{48}Ni [13] allowed to establish 2p radioactivity as a new nuclear decay mode. These experimental findings could be compared to model predictions from different theories [14–16], which were found to be in reasonable agreement with the experimental results. However, for a more detailed study in particular of the dynamics of 2p radioactivity, more exclusive observables like the individual proton energies and the relative proton-proton angle have to be measured. This requires the direct observation of the two protons.

We developed a new detection setup which is based on the principle of a time-projection chamber (TPC). In such a setup, the ions of interest are implanted in a gas volume where, with a characteristic half-life, the radioactive decay

of these isotopes takes place. This chamber then allows to correlate in space and in time the implantation and the decay. In addition and due to the relatively long range of the protons in gas as compared to silicon detectors, the charges produced due to the slowing down of the protons can be visualised and the proton traces can be reconstructed in three dimensions. Figure 1 shows schematically such a TPC.

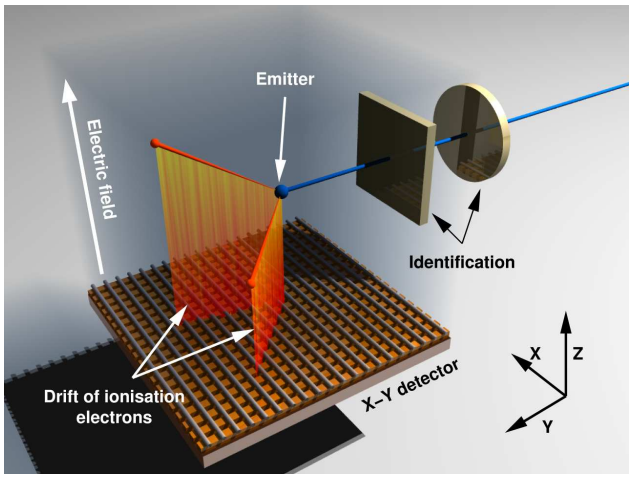

Fig. 1. Schematic representation of a time-projection chamber for 2p events. The isotopes of interest are identified by means of their time of flight and their energy loss with silicon detectors at the entrance of the chamber. The energy of the isotopes is adjusted to stop them in the active volume of the TPC where their decay takes place with a characteristic half-life. The electrons produced by the slowing down of the ions and of the protons emitted drift in the electric field of the TPC towards a set of four gas electron multipliers (not shown) where they are amplified and finally detected in a two-dimensional detector consisting of X and Y strips.

2. General description of the time-projection chamber

2.1. *Geometrical dimensions and main components*

The TPC is housed in a chamber of size 60x60x60 cm^3. The TPC in its present version has an active volume of 15.4x15.4x6 cm^3. However, due to the electric field configuration, the 15 strips corresponding to 6 mm on either side collect only few electrons and the effective active volume is only about 13.8x13.8x6 cm^3. A beam pipe with an entrance window of 250μm of aluminium brings the vacuum as close as possible to the active volume of the detector. This window is located at about 2 cm of the active volume. The beam entrance is at a height of about 3 cm above the first gas electron multiplier (GEM), which allows all protons from 2p events to be stopped in the gas before reaching any other material.

Alpha sources can be installed either inside the active volume of the detector or just outside. In particular, a triple-α source is permanently mounted during operation on a circularly moving arm above the drift cathode of the TPC. Fixed collimators included in this cathode allow to detect α particles with fixed and well-defined angles in the chamber. Therefore, calibrations of the angles of trajectories which are directly related to the drift velocity of the charges in the gas can be performed at any moment. In addition, the detector resolution can be verified on-line.

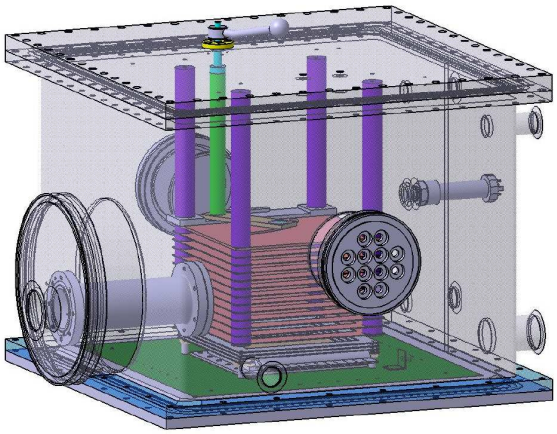

Fig. 2. Three-dimensional view of the TPC showing the housing of the TPC and the drift electrodes. The quarter circle in the cathode shows the possible movement of the permanently installed α source. Below the drift electrodes, four GEMs and the 2D detector are visible. All these parts are mounted on the electronics mother board on the bottom of the chamber. The beam entrance is from the left. Flanges for high-voltage connectors, pumping, and vacuum gauges are also indicated.

An electrical field between the detector cathode (top in figure 2) and the detection part (bottom part) makes the electrons created by charged particles in the P10 (90% Ar, 10% CH_4) detection gas drift towards the detection plane. The electron signal is amplified by multiplying the electrons in a set of four GEMs. These GEMs have a distance from each other of 3 to 10 mm. The last GEM has a distance of 10 mm from the two-dimensional detector.

The detection plane is a micro-groove detector [17]. It has two sets of orthogonal strips for the X and Y directions. For either direction, one out of two strip is read out by ASIC electronics, whereas the other half is grouped in packages of 64 strips and read out via standard electronics by means of a charge-integrating preamplifier and a shaper.

2.2. *Read-out electronics of the TPC*

The GEMs are read out by standard electronics. Via preamplifiers they are connected to shaping amplifiers. They allow the measurement of the total energy of any event inside the active volume of the detector. This part will not be described in more detail here.

The strips are connected on one end only via flexible printed circuits to connectors which allow to pass the signals from the inside of the detector to the outside of the

chamber by means of a mother board, on which the 2D detector is mounted. The readout changes from one side to the other from each strip to its neighbour. We used this property to send the strips readout on one side of each face of the 2D detector to ASIC chips, whereas the strips readout on the opposite side were grouped together in groups of 64 strips and send to standard charge-sensitive preamplifiers and shapers.

This reduces the number of electronics channels with ASIC readout by a factor of two and still yields sufficient "granularity" for the resolution effectively obtained and needed as compared to the track length of events of interest. Thus for an active detection surface of 15.4x15.4 cm^2 and a channel to be readout every 400μm, this yields 384 ASIC channels for each face of the 2D detector. In total, 12 groups of 64 channels are read in parallel (figure 3). Each of the channels readout individually has an energy and a timing branch which are extracted in parallel. The first channel which fires triggers the whole readout process. The timing of all channels is given with respect to this channel.

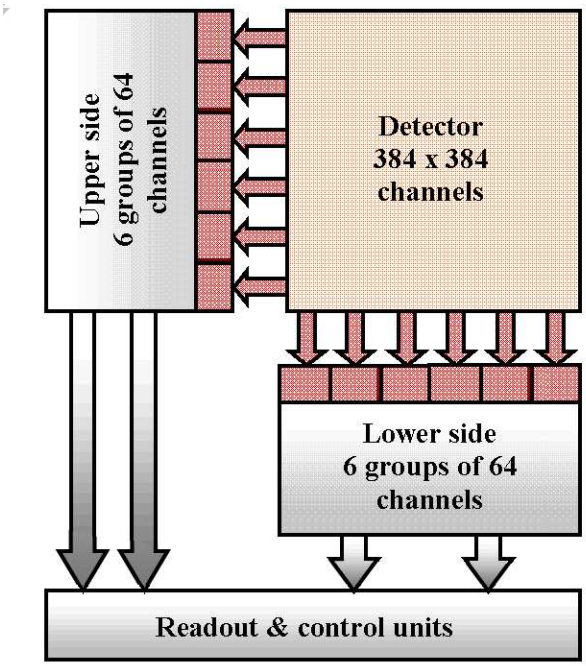

Fig. 3. The figure shows the general layout scheme of the detector and its coupling to the ASIC electronics. The upper and lower parts of the detector are read out in six groups of 64 channels each.

As shown in figure 4, the electronic is composed of two main distinct parts: analog treatment and digital processing. Each of the six groups of 64 channels is connected on a backplane with an analog bus and a digital bus. The digital bus allows to chain groups of channels and is controlled by a PXI system. The analog bus carries the triggering values and the six times 64 differential values of energy and timing. For the whole detector, 768 energy and 768 time channels have to be treated. This is done by means of the VA/TA ASIC from IDEAS [18]. These chips have a dynamical symmetric range in the energy channels of $\pm$ 1.5 pC with a non-linearity of 2%.

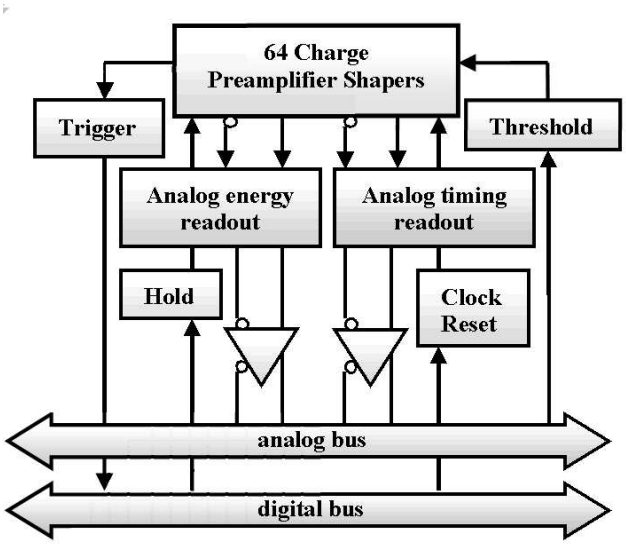

Fig. 4. The figure shows the main functions of the front end electronics.

The noise is 3100 e- + 3.3 e- /pF for typical biases [18]. The total time range is 10μs with a non-linearity of 0.1%. Each VA ASIC has 32 energy channel. Each TA ASIC has 32 timing channel. Two VA and two TA chips are mounted on a daughter board (figure 5).

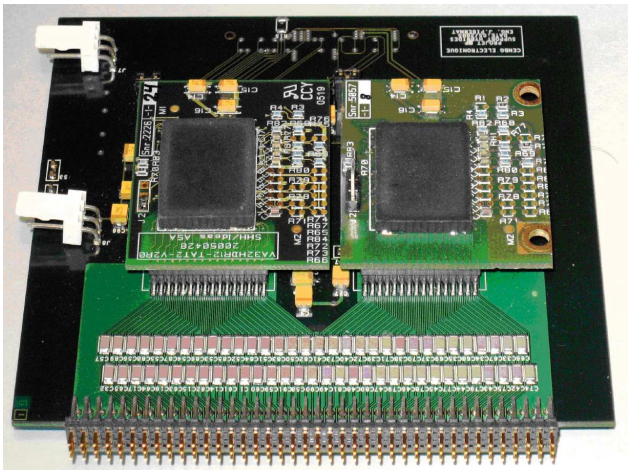

Fig. 5. The photo shows a daughter board on which two 32-channel ASIC chips are mounted. Each board thus can handle 64 energy and 64 time channels.

Each analog bus ends with a circuit to adjust levels and impedances (figure 6). Out of this board, 384 differential signals for energy and 384 differential signals for timing of one side of the detector are available for digitazing. A local trigger signal from one face of the detector is also available. Each digital bus ends with a PXI module (figure 7). This module manages the timing by keeping operations for analog signals provided by the ASIC on the one hand and by pilot reading these signals (time and energy) for encoding on the other hand. The PXI system is driven by a real-time

CPU 8145-RT and is equipped with two I/O modules and analog encoders NI-6070E [19]. The PXI equipment allows to fully control the system and treats the differential signals of time and energy for visualization and local storage if required.

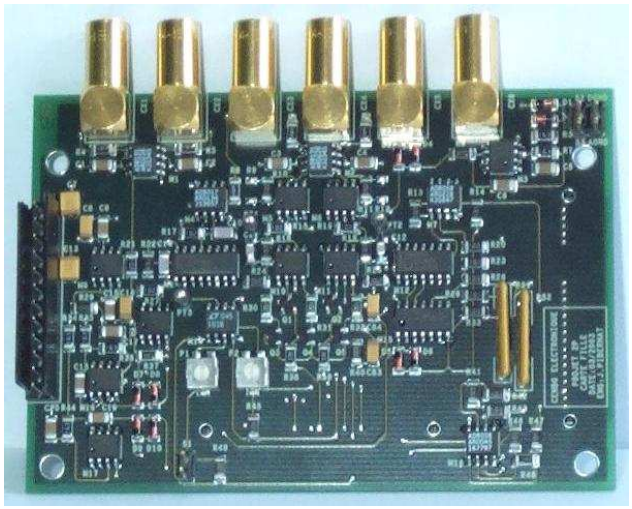

Fig. 6. Interface board to adapt signals from the ASIC for differential transmission to the digitazing units.

The logic of PXI sequencing and control of the hardware is integrated into FPGAs. The system is flexible in many ways and can be extended to a detector with more lanes. However, it should be noted that the time dedicated to reading channels depends on the number of lanes.

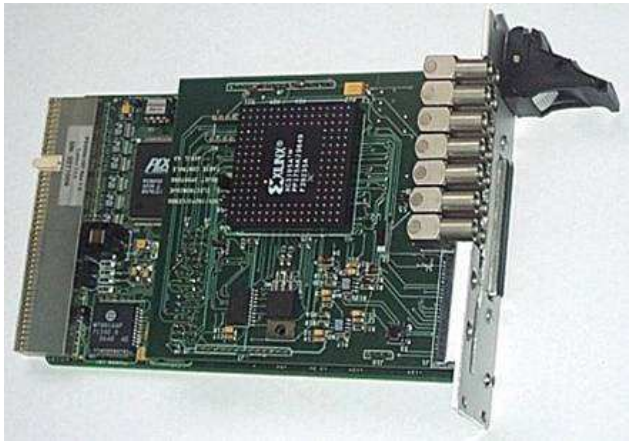

Fig. 7. One of the two PXI boards for control and command.

For experiments, the PXI prepares the signals to be fed into VME modules (CAEN C-RAMS). The VME modules are conducted by the GANIL data acquisition system and their data are included in the data stream of others VME and VXI modules. The readout of the analog signals is gouverned by a 1 MHz sequencer which assures a fast data transfer from the ASIC to the VME modules across the interface boards. The bottleneck is the readout from the VME crate into the data acquisition system. For about 1550 channels per event (1536 from the ASIC electronics and some 25 channels from the 64-channel groups, the GEMs and the beam-line detectors), we obtain 1.3 ms of dead time per event.

3. Characteristics and performances of the TPC

In the following sections, we will describe the performances of the different components of the detector as tested with a triple-α source. These measurements allowed the GEM energy resolution and the GEM gains to be determined. We could also test the long term stability of these parameters. The two-dimensional detector was investigated in terms of its position resolution, its position precision, and its energy resolution. The drift-time analysis allowed the third dimension of the TPC to be explored. Finally, we will describe the off-line calibration scheme.

3.1. *Gas electron multipliers*

Gas electron multipliers [20] have been developed in order to amplify the signal produced by ionising particles in gas detectors. The GEMs used in our setup have a total size of 15x15 cm^2 and are subdivided in two halves. They consist of a kapton layer of 50μm thickness covered on both sides with a copper surface (5μm). The hole diameter of the GEMs is 70μm with a distance of 140μm between two hole centres. The GEMs are mounted on an epoxy frame of thickness 2.54 mm.

When approaching a GEM, the electrons are focussed in the holes of the GEM. Due to strong electric fields in the holes from a potential difference between the two sides of the GEM, the electrons are multiplied by avalanches and a number of electrons increased by the gain of the GEM leaves the GEM.

In our TPC, the electrons produced by the slowing down of the charged particles in the gas drift in the electric field (typically 210 V/cm) of the detector towards the GEMs and the two-dimensional (2D) detector. These electrons are multiplied by a set of four GEMs. The gain of the GEMs depends on the voltage applied across them, the nature of the gas, the gas pressure, and the distance between the GEMs. This last dependence is due to the possibility of electrons drifting back to the GEM where they were produced and depends sensitively on the drift voltage between the GEMs.

In our present implementation, we use different power supplies for each GEM. The voltage difference between the upper and lower part of the GEM is ensured by a passive resistor chain. The charge signal of the upper and lower part of the GEM can be coupled out via a capacitor and enables us thus to determine the total energy of a decay event from the signals of the different GEMs.

Figure 8 shows the energy distribution as determined with a triple-α source (^{239}Pu, ^{241}Am, ^{244}Cm). On all GEMs, the three different α-particle energies can be clearly distinguished and resolutions between 120 and 200 keV are routinely reached.

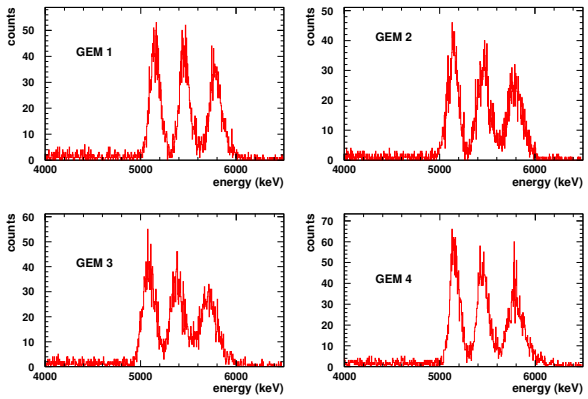

Fig. 8. Energy resolution as obtained with the gas electron multipliers and a triple-α source. For these measurements, the source was mounted inside the active volume of the TPC. The α particles were collimated with a collimator of length 3 mm and an opening of 1 mm. The figure shows the spectra obtained after a charge-integrating preamplifier and a shaper. The voltage over the GEMs was 320 V for each GEM and the drift voltage between the GEMs and between the last GEM and the 2D detector was 92, 104, 121, and 141 V, respectively. The distances between GEMs as well as between the last GEM and the 2D detector was 3 mm. The measurement was performed at 500 mbar of P10.

The GEM gain was measured in a simplified setup. For this purpose, we mounted only two GEMs with different distances. Three different gas pressures (500, 750, and 1030 mbar) were used. Only measurements with P10 gas, a 90% argon - 10% methane mixture, were performed. The gain was defined as the ratio of the signals observed at the lower side of the second versus the first GEM. As shown in figure 9, the gain increases with the voltage applied over the second GEM (the voltage of the first GEM was kept constant). The voltage was increased until reaching the sparking region. Similar gains were obtained for all pressure regimes, however, with increasing pressure at increasingly high voltages (see figure 9). These gains compare well with the gains determined by other groups (see e.g. [21,22]). However, most likely due to impurities in the gas (for example moisture) and the use of highly-ionising α particles, the sparking regime was reached earlier in our application. Online we use typically a voltage across the GEMs of 300 V at 500 mbar.

The mutual influence of the GEMs is clearly seen when comparing the figures obtained for different GEM distances. This effect can possibly be reduced by more carefully adjusting the drift voltages between the GEMs and thus preventing electrons to return to the GEM where they were produced. As we can without any significant loss work at distances of 5 or even 10 mm, we did not try to improve this aspect.

In the online configuration, we work typically with a total gain of 50000 to 100000. As discussed below the total gain has a slight influence also on the position resolution obtained on the 2D detector. However, the loss of resolution for larger gains and larger distances between the GEMs

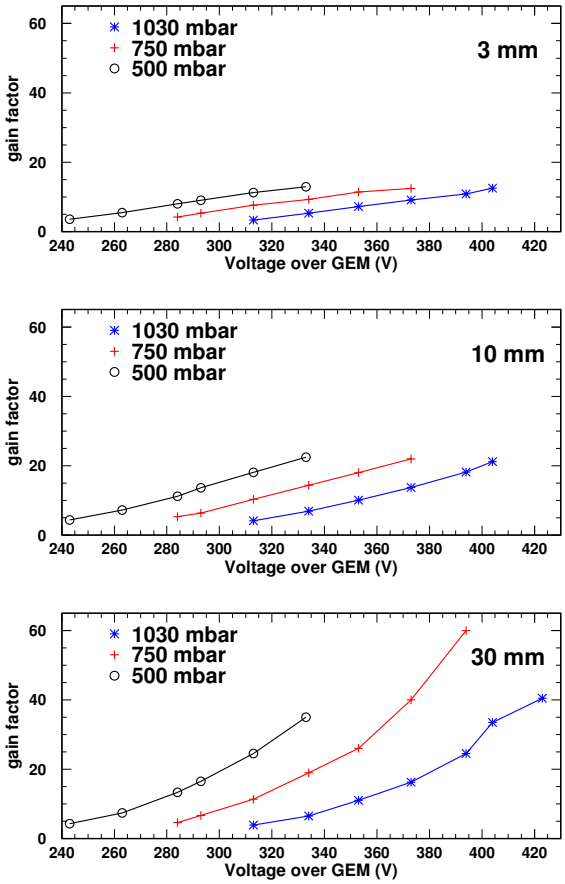

Fig. 9. The figure shows the gains measured for different GEM configurations. Three pressure regimes were studied and three GEM distances were used. The gains were measured with two GEMs and are defined as the ratio between the signals measured on the second GEM and the first GEM. From the top to the bottom figure, the distance between the GEMs was changed from 3 over 10 to 30 mm.

was not considered important for our purpose. Therefore, we adopted a distance of 10 mm between the GEMs as well as between the last GEM and the 2D detector and voltages of 300 V across the GEMs.

The overall stability of our chamber was tested by measuring the pulse height stability of the GEMs over a period of almost a week. Figure 10 shows the signal obtained from one of the GEMs with a triple-α source. The figure presents the signal height as a function of time. The relative gain stability thus determined is about 2%. This stability is comparable to the resolution obtained for short accumulation times of 150-200 keV for α particles of 5.5 MeV and does therefore not significantly influence the properties of the TPC.

As will be shown below, the GEMs enable us to obtain sufficiently high gains to detect the low-energy protons from 2p radioactivity events (typical energy of each proton of 550 keV) at the same time as the signals from high-energy events from heavy-ion implantation (typical energy 200-250 MeV). The gains ensure that the charges detected by each strip of the 2D detector are high enough to trigger

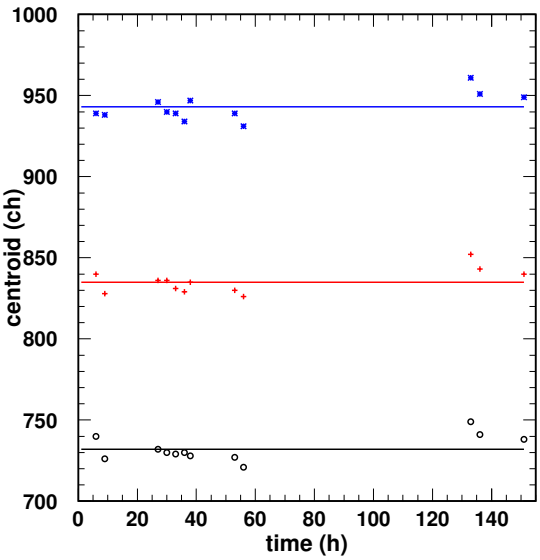

Fig. 10. Signal height as measured from one GEM as a function of time for an observation period of about one week. The plot shows the centroids of the three α-particle energies of a triple-α source. The gain stability of about 2% may be compared to the energy resolution obtained for short measurement times of 2.5 - 3.5%.

each individual strip which is necessary for a measurement of the arrival time of the first electrons on each strip (see below).

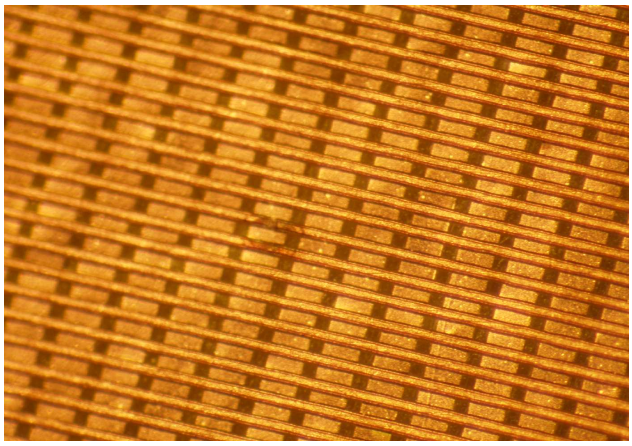

Fig. 11. Photo of the 2D detector composed of a copper-coated kapton foil of thickness 50μm on which the strips have been etched on the upper and lower side. The top strips have a pitch of 100μm and a width of 50μm and are connected on both ends two-by-two. The lower-side strips have a pitch of 200μm and a width of 150μm. The copper thickness on both sides is 5μm.

3.2. *Characteristics of the 2D detector*

The 2D detector is a micro-groove detector [17]. The strips on the upper side are orthogonal with respect to the strips on the lower side (see figure 11). The detector consists of a copper coated kapton layer of thickness 50μm. The strips are etched into the copper surface. The top strips have a width of 50μm and a pitch of 100μm. They are connected together two-by-two on both ends. This was meant to increase the gain of the 2D detector when a high voltage is applied between the two strip sides. However, in the present application no high voltage is applied between the two sides (see below).

The lower side of the detector consists of strips with a pitch of 200μm and a width of 150μm. The kapton between the two strip layers is partially removed to allow the charge collection on the top and the bottom side. As the surfaces of the strips are not the same on both sides, a small voltage (typically 10-20 V depending on the high-voltage settings of the TPC) has to be applied to equilibrate the charges collected on both sides [23]. Besides this voltage, the 2D detector is at ground potential.

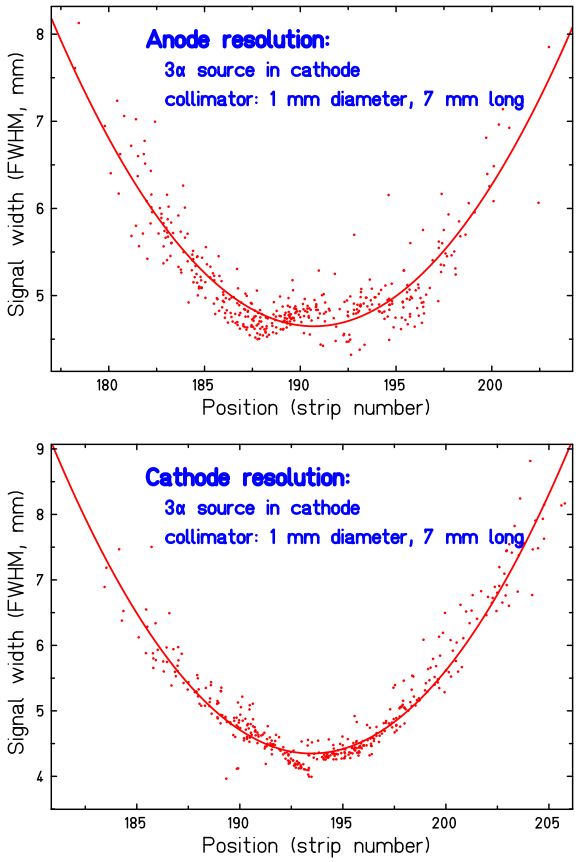

Fig. 12. The figure shows the position resolution obtained with a strongly collimated α-particle source as described in the text. The figures show the width of the single-event signal distributions as a function of the strip number on which the maximum of the Gaussian distribution was determined by the fit. The minimum is reached when the maximum is on the strip above which the source was mounted. In this case, the trajectories point straight to the detection plane with an angle of 90^o between the trajectory and the detection plane. A typical distribution width for single events is of the order of 4-5 mm.

The position resolution of the 2D detector has been determined in two distinct ways. A strongly collimated α-

particle source was mounted in the drift cathode and the widths of the single-event distributions of the signals as detected on the upper and lower strip planes were determined. The smallest width can then be associated with α-particle traces pointing directly to the detector plane (90^0 with respect to the detection plane) and yield therefore directly the resolution. The results from this approach are shown in figure 12. A resolution of typically 4-5 mm was determined for the 2D detection setup. This resolution has to be compared to typical track lengths of 2.3 cm at 500 mbar gas pressure for individual protons from two-proton radioactivity with an energy of 550 keV.

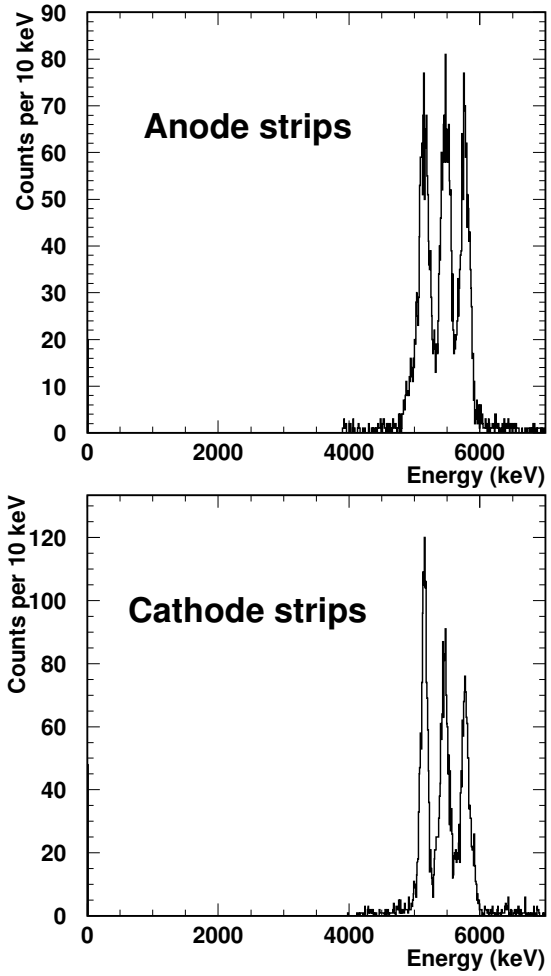

Fig. 13. The figure shows the energy resolution obtained with a collimated triple-α source positioned on the side of the active volume. The α particle penetrate in the active volume and are completely stopped in the active part of the gas volume. The energy signal of all strips is summed and plotted. This result is obtained after the gain matching described below. A typical resolution of 150 keV is routinely achieved.

However, in this measurement, the degradation of the resolution in the drift section of the detector and due to the GEMs is included. Therefore, measurements have also been performed with a one-millimetre hole in a plastic plate which could be positioned at different heights in the drift section, from 6 cm to zero in which case the plastic plate is directly on the first GEM. The one-millimetre opening was subtracted quadratically from the resolutions measured. This approach yielded results similar to the previous one.

Another information obtained during the α-particle tests, with the source mounted in the cathode plate and pointing vertically downwards, is the precision with which the maximum of the single-event distributions can be determined. Due to the fact that the signal is distributed over about 20 strips, precisions far below the strip pitch (400 μm for those read out by the ASIC electronics) could be found when fitting the distributions with a Gaussian, a typical value being 180μm.

The energy resolution of the strips can be determined by summing up all charges collected on the different strips. As the α particles are completely stopped in the gas, full-energy peaks should be observable. Figure 13 shows the spectrum thus obtained with a triple-α source. The three α lines are nicely separated and a resolution of about 150 keV is achieved routinely.

3.3. *Gain-matching of the strips*

As mentioned above, the TPC has a total of 1536 energy and time channels half of them being coupled to ASIC electronics. The signal collected on the different detector strips and the gains of the different ASIC chips can be rather different. Therefore, a precision calibration in energy but also in time is necessary to gain match the different channels.

In the experiment we performed with the TPC (see below), we used two methods to perform this gain matching. First, an offline matching was performed by injecting a pulser signal in the lower side of the last GEM. This signal creates an image charge on the strips in both directions, which allows establishing an energy calibration curve for each strip. The time matching was performed with the same signal by delaying the "hold" signal (see paragraph 2.2.) for the readout.

This method yields a satisfactory result for the time channels. However, for the energy channels, the signals detected with real events were not as uniform as expected. This might be for example due to slightly varying sizes of the strips and thus varying charge collection. Therefore, we performed a correction, where we used the primary as well as fragment beams which traversed the whole chamber with relatively high energy. This allows to assume that the energy loss per range unit does not change and thus all the strips are supposed to collect the same charge. The different beams yielded different signal heights thus allowing to establish a correction curve for each strip. To calibrate the strips parallel to the beam direction, we rotated the chamber after the experiment and performed a similar scan. Figure 14 shows the signal from an implantation event on the strips perpendicular to the beam direction without calibration, with the pulser calibration and with the additional

correction.

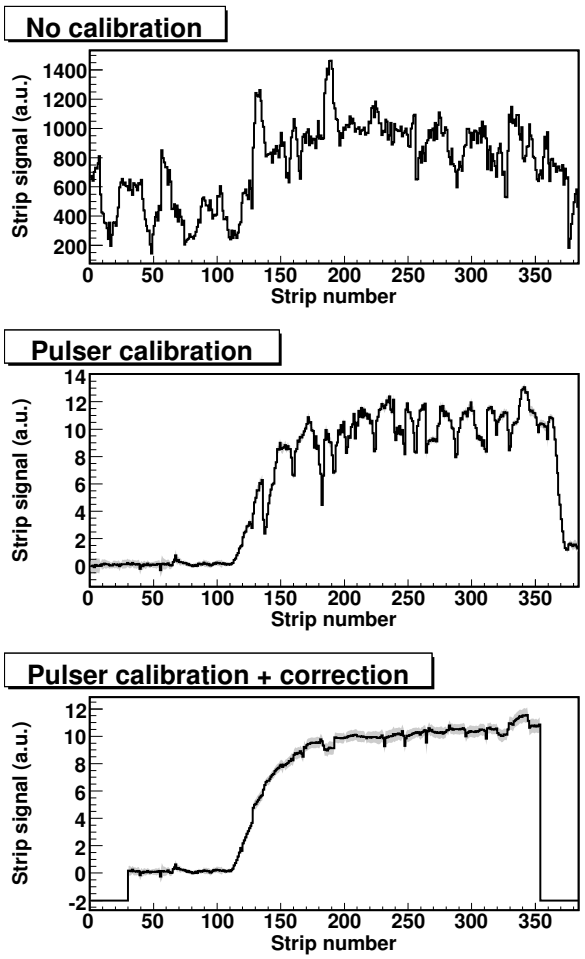

Fig. 14. The signal registered by each strip perpendicular to the beam is shown for an ion implantation event. The upper spectrum shows the ASIC response without calibration, the center spectrum with the pulser calibration described in the text, and the lower figure with the additional correction by means of the traversing beams. The smoothing procedure is not yet applied for these spectra (see section 4.1. for details).

3.4. *Drift-time characteristics*

The drift-time analysis is used to determine the position in the direction of the electric field of the chamber. In our application, this drift-time analysis serves to analyse the angle of the proton tracks with respect to the detection plane. The electrons produced by the energy loss of charged particles drift towards the detection plane with a constant velocity depending on the nature and the pressure of the gas used and the electric field of the drift zone. The electrons created closer to the detection plane arrive first on this detection plane, whereas electrons produced higher above the two-dimensional detector arrive with some delay. With the known drift velocity, the time delay can be transformed into a distance and thus in an angle of the track.

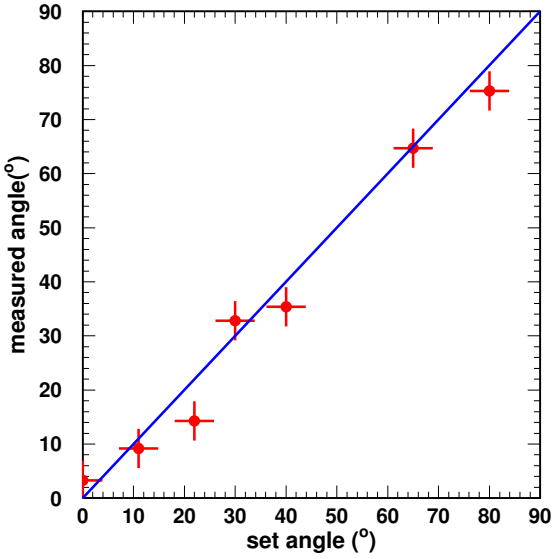

Fig. 15. Drift time calibration as performed with α particles entering the detection volume under fixed angles. With the drift time which depends on the nature of the gas, its pressure and the drift voltage, the time delay between the strips can be converted into a drift distance and thus into an angle of a trajectory with respect to the detection plane. The angle resolution obtained is 7-8^o. The full line is to guide the eye and represents the expected correlation.

In figure 15, we show the calibration curve determined with α particles entering the detector with a fixed angle. A linear dependence between the entrance angle and the angle determined in the analysis of the drift time is observed. The angle was determined by a measurement of the arrival time difference of the charge cloud on the different strips. By means of the electron drift velocity in the gas, which depends on the pressure (500 mbar), the drift voltage (about 200V/cm), and the gas type (90% Ar - 10% CH_4), the angle of the α-particle trajectory could be determined. Under online conditions, this correlation is measured with an α source integrated in the drift cathode which can be moved in front of several collimators with well defined angles.

However, in most of the events the electronics does not give a continous drift time curve, but rather the curve has several separated parts, as if some electronics channels got a later start than others. The reason for this is not quite clear to us. Nonetheless, we developped a procedure which allows to cure this problem. In the analysis the different parts are fit with a single straight line using different offsets for the different parts, but the same slope. Figure 16 shows two correlated events of an ion implantation followed by a radioactive decay via proton emission. The upper part shows the implantation energy signal on the X and Y planes, whereas the other plots show the decay event: the energy distribution on the different strips as well as the drift time differences. The lowest part is a zoom on the interesting part of the spectrum.

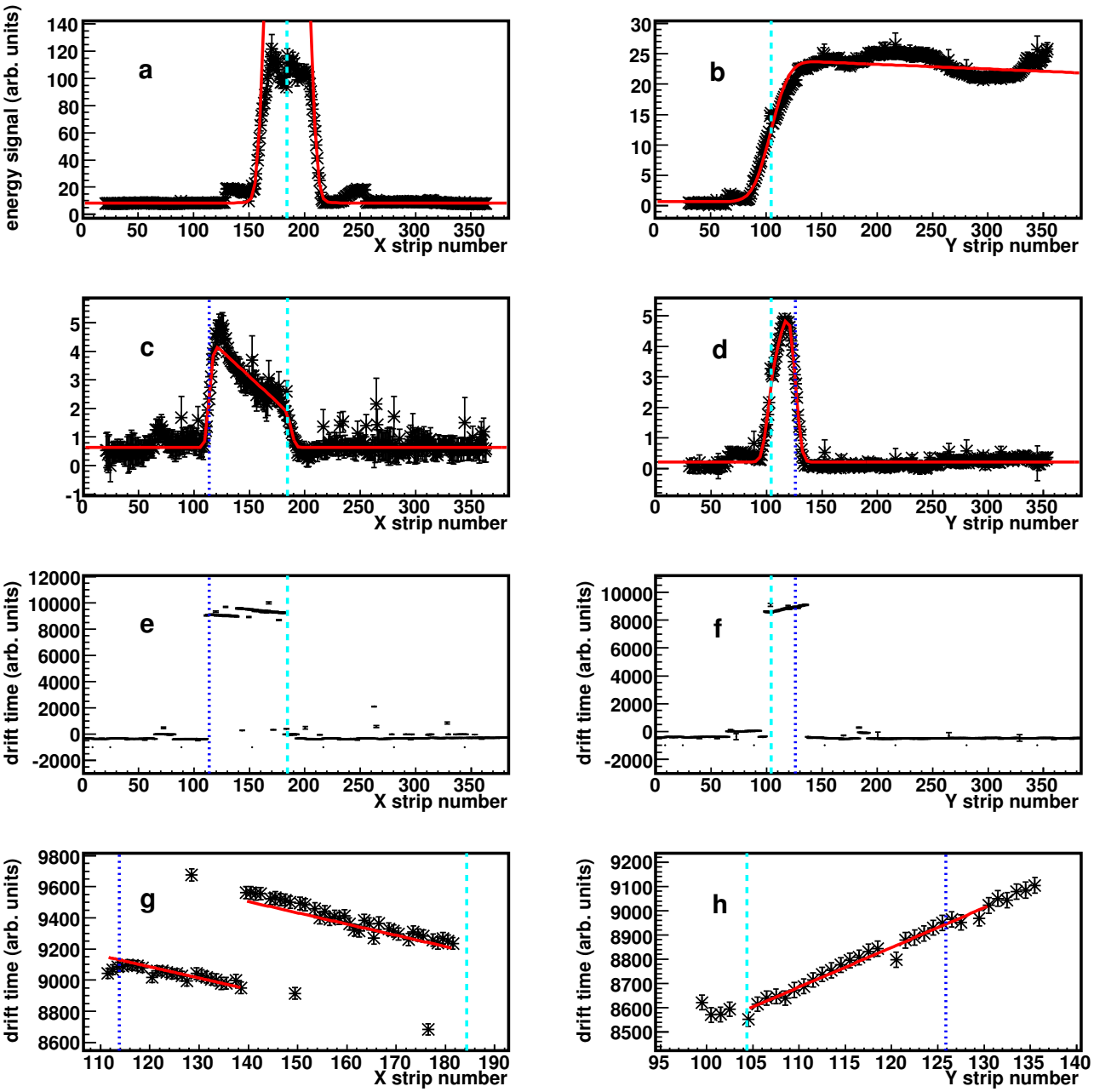

Fig. 16. Correlated implantation and decay event for ^{52}Ni. The most upper graphs (a,b) show the energy distribution of the implantation event on the X and Y planes. The solid (red) line is the fit of the implantation profile. On the X plane, the central part is not fit (Gaussian profile) due to saturation effects. The dashed line (light blue) gives the implantation position determined. The next two panels (c,d) present the energy distribution of the decay event. The solid line (red) is again the result of the fit with our theoretical curve (straight line convoluted with a Gaussian). The dashed line (light blue) is the starting point of the trajectory, whereas the dotted line (dark blue) is the stopping point of the trajectory. The four lower panels show the drift-time distribution obtained for the particle emitted (e,f) and a zoom of the same spectra on the interesting parts (g,h). The solid line (red) shows the drift-time fit (see text).

4. Selected online results

After a first online test of the detector at the LISE2000 beam line of GANIL in April 2006, the TPC was used for the first real data taking in September 2006 [24]. Figure 17 shows the TPC installed at the LISE3 beam line of GANIL. The aim of the experiment was to observe directly the emission of two protons in the decay of ^{45}Fe. To calibrate the detector and to check its online performances, the LISE3 beam line was set to select ^{52}Ni at the beginning of the experiment. This nucleus is a known β-delayed proton emitter with proton energies around 1.3 MeV [25]. Calibrations performed with this spectrometer setting will be described in the following section. The setting on ^{45}Fe finally allowed to unambiguously identify the two protons emitted from the ground state of this nucleus as well as β-delayed two-

proton emission from ^{43}Cr, a nucleus selected at the same time as ^{45}Fe. These results will be presented schematically at the end of this chapter.

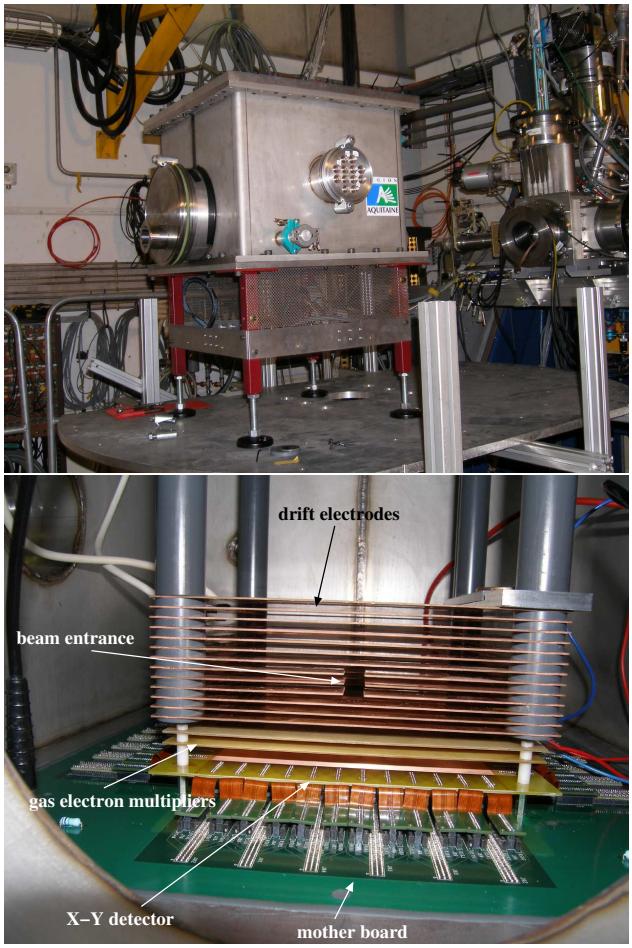

Fig. 17. Top: The TPC installed at the exit of the LISE3 beam line of GANIL. Bottom: The interior of the TPC. The beam entrance hole in the drift frames as well as the electronics mother board with the printed circuits connecting the micro-groove detector to the mother board can be seen. The version of the TPC shown is one with only two GEMs.

4.1. *Calibrations performed with ^{52}Ni*

As just mentioned, ^{52}Ni is a βp emitter. This allows to use this nucleus to test whether the end of an implantation track corresponds to the beginning of the decay track from the emitted proton. For a one-proton event, this information is easy to be obtained. In a two-proton emission, it is essential that the proton tracks can be assumed to start at the same position where the implantation track ended.

To perform this analysis, the energy signal from the different strips is first calibrated (see paragraph 3.4.). In a second step, we performed a smoothing of the energy signals. For this purpose, the energy signal of a channel is redistributed over five channels, two to the left, the channel itself, and two to the right with weights of 1:3:6:3:1. We do not lose any significant information due to this smoothing, as the position resolution of the TPC is a factor of 2-3 larger (4-5 mm) than the range of this smoothing (2 mm).

In a next step, the implantation signals are fitted with a function which is a folding of a straight line and a Gaussian for the strips perpendicular to the beam direction and with a Gaussian for the strips parallel to the beam. The decay events are fitted with the same function of a folded straight line and a Gaussian. We tested this procedure also with a parabola instead of the straight line, however, without any significant gain. This function approximates the distribution due to the Bragg peak for the energy loss of charged particles. The end of the implantation track is defined at about 1/2 of the Gaussian height. The same is true also for the start and the end of the proton track.

Figure 18 shows the start of the proton track plotted as a function of the end of the implantation track thus determined for the strips perpendicular to the beam direction (upper part) and parallel to the beam direction (lower part). For the first plot, a nice correlation is obtained. The scatter observed reflects the position resolution of the TPC. For the strips parallel to the beam direction, the correspondence is not as good. This is mainly due to the fact that for events where the ions were implanted deeply in the chamber, the different strips parallel to the beam direction collect rather large amounts of charges. Therefore, the ASIC channels often saturate and the determination of the implantation point in this direction is rather difficult. We will show below, how this problem can be overcome in the future.

In future experiments, ^{52}Ni can also be used to check the energy calibration of the TPC and even to test its resolution. ^{52}Ni mainly emits protons with energies of 1.06 MeV and 1.35 MeV [25]. The energy of these proton lines is in the same range as the total energy release of a 2p event from ^{45}Fe. In addition, under good experimental conditions, the TPC via the energy signal of the GEMs should allow to resolve the two proton lines of ^{52}Ni. In the experiment performed in September 2006, important noise on the GEM signals did not allow to perform these tests.

4.2. *Selected results obtained with ^{43}Cr and ^{45}Fe*

In the September 2006 run, we obtained implantation and decay events for 10 ^{45}Fe ions [24] and several hundred implantation-decay couples for ^{43}Cr. A detailed analysis of these events is under way. The ^{43}Cr data will allow us to test the performances of the detector and in particular to check, whether in this case the angle between the two protons will be isotropically distributed as expected for a sequential decay. The data for ^{45}Fe should allow a rough first comparison between the experimental distributions and theoretical predictions.

Figure 19 shows several correlated implantation and decay events for ^{45}Fe. Similar information is shown in figure 20 for β2p decays of ^{43}Cr. As the energy of these β2p events is much higher than the one of ^{45}Fe 2p events, most

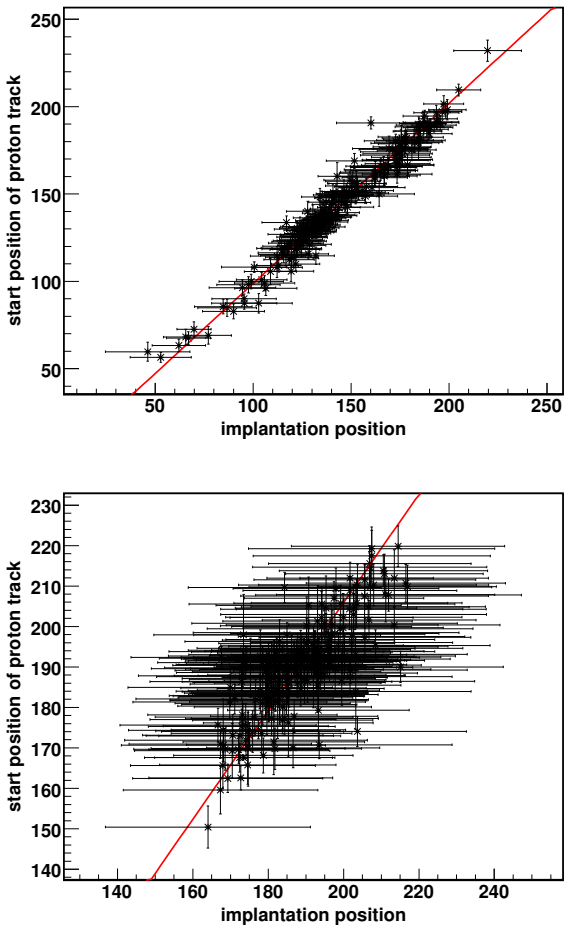

Fig. 18. Top: Correlation between the end of the implantation track and the beginning of the proton track for the strips perpendicular to the beam direction. Bottom: Same as top figure but for the strips parallel to the beam direction. The lines are fits to the experimental data.

of the protons have too high energy and leave the active volume of the chamber before being stopped.

From these figures, the decay trajectories can be determined. Figure 21 show a two-dimensional view of a 2p event from ^{45}Fe.

5. Conclusions and outlook

We described the basic performances as obtained with a time projection chamber built at the Centre d'Etudes Nucléaires de Bordeaux-Gradignan. The aim of this TPC is the study of two-proton emission either from nuclear ground states as in the case of ground-state two-proton radioactivity of e.g. ^{45}Fe or from excited states populated by nuclear β decay as e.g. in the case of ^{43}Cr.

The signals produced either by heavy-ion implantation events or by proton emission events are first amplified by a set of four gas electron multipliers and detected by a two-dimensional detector consisting of two orthogonal sets of 768 strips. Every second of the strips is read out by means

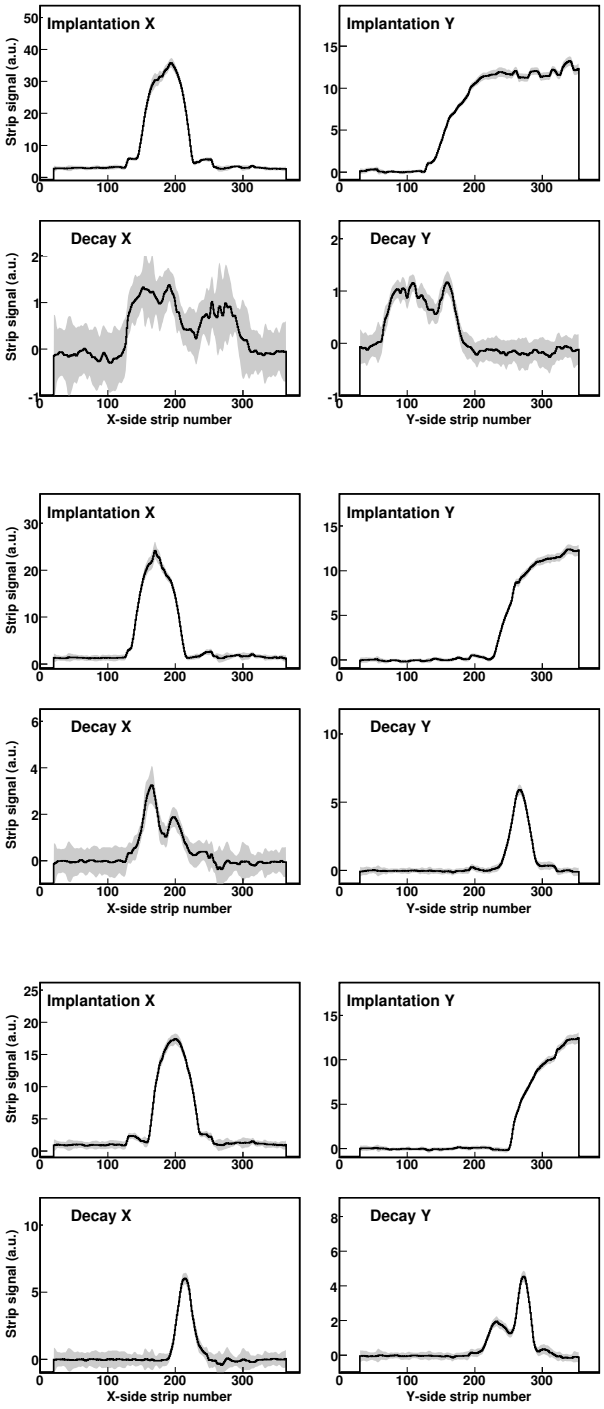

Fig. 19. Three implantation and correlated decay events are shown for ^{45}Fe. The figures show each time the implantation energy signal on the X and Y strips and the decay energy signal on the same strips just below. The decay events start where the implantation trajectory ends. In all cases, the tracks of the two protons can be clearly seen. The gray region indicates the uncertainties of the energy signals for each channel.

of ASIC electronics. The third dimension of the events is obtained by time projection of the tracks in the detector gas. This allows visualising events in three dimensions.

The performances described show that the detector is capable to detect 2p events and to determine their basic

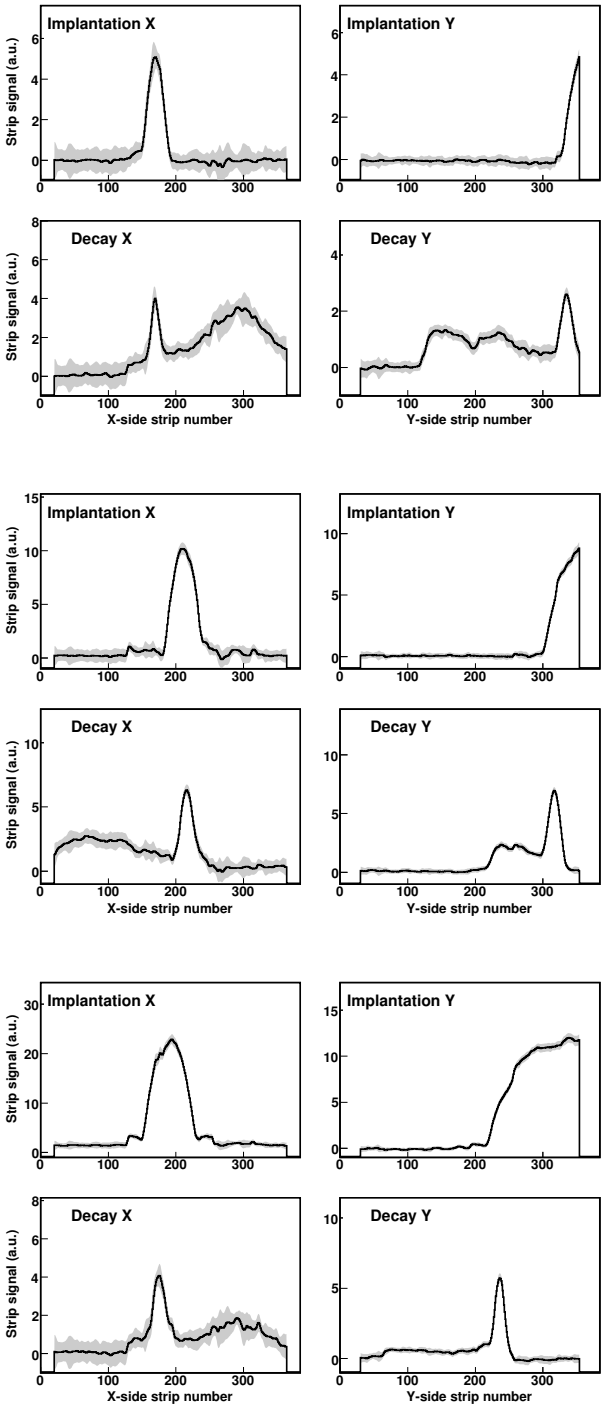

Fig. 20. Same as figure 19 but for β2p emission from ^{43}Cr. The energy of the protons emitted in this decay is much higher than for protons emitted from ^{45}Fe 2p decay and most of the protons leave the active volume of the chamber before being completely stopped. The energy loss of the electron from β decay is too small to be visible.

characteristics such as the energy of the protons and their relative angle. A first experiment with this detector demonstrated its performances.

Several improvement of the detector are under way. First of all the entrance direction of the beam will be modified to an entrance angle of 45^0 with respect to the two strip directions. This has several advantages: i) Both strip sets can be calibrated with traversing beams without rotating the detector. ii) The saturation effects observed for the strips parallel to the beam entrance will be cured, as the charges will be distributed on many more strips. iii) The effective range distribution of the heavy ions to be stopped in the chamber will be increased by $\sqrt{2}$ and 100% of the ^{45}Fe ions will be stopped in the active volume of the TPC.

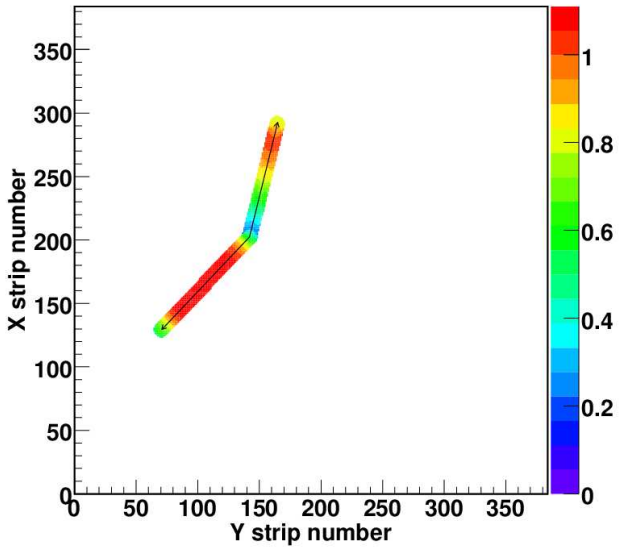

Fig. 21. Two-dimensional projection of a ^{45}Fe event as reconstructed from the strip information in X and Y. The colour code is indicative of the energy loss detected by the strips. This plot shows the first event of figure 19.

The second modification concerns the height of the active volume of the TPC. In the September 2006 experiment, the height was only 6 cm, sufficient to stop all protons from two-proton radioactivity of ^{45}Fe. However, as mentioned β2p events from e.g. ^{43}Cr have much higher energies and are only rarely stopped in the TPC. An increase in height allows to stop more of these protons, at least in cases where the proton direction points mainly upwards. Another possible upgrade is to modify the chamber to be able to work at higher pressures.

Finally, a flash ADC will be added on two of the GEM signals. This allows to get access to the time evolution of the signals collected by the GEMs and will help to reconstruct the decay signal in three dimensions. In the present setup, two-proton emission with the two protons emitted in the same direction and perpendicular to the detection plane can not be distinguished from an emission pattern where the two protons are emitted back-to-back, again perpendicular to the detection plane. The duration of the signal as measured with the flash ADC will allow to distinguish these two events.

The present detector is similar to an optical time-projection chamber developped in parallel at Warsaw University [26] for the same purpose.

Acknowledgment

We would like to thank the whole GANIL and in particular the LISE staff and the GANIL DAQ group for their help in the preparation phase and during the experiment. This work was supported by the Conseil régional d'Aquitaine and the European Union via the EURONS/ACTAR contract and through the Human Capital and Mobility programme.

References

[1] V. I. Goldansky, Nucl. Phys. **19**, 482 (1960).
[2] B. A. Brown, Phys. Rev. C **43**, R1513 (1991).
[3] W. E. Ormand, Phys. Rev. C **53**, 214 (1996).
[4] B. J. Cole, Phys. Rev. C **54**, 1240 (1996).
[5] B. A. Brown, F. C. Barker, and D. J. Millener, Phys. Rev. C **65**, 051309(R) (2002).
[6] B. Blank *et al.*, Phys. Rev. Lett. **77**, 2893 (1996).
[7] B. Blank *et al.*, Phys. Rev. Lett. **84**, 1116 (2000).
[8] J. Giovinazzo *et al.*, Eur. Phys. J. **A11**, 247 (2001).
[9] J. Giovinazzo *et al.*, Phys. Rev. Lett. **89**, 102501 (2002).
[10] M. Pfützner *et al.*, Eur. Phys. J. **A14**, 279 (2002).
[11] B. Blank, AIP Conf. Proc. **831**, 352 (2006).
[12] B. Blank *et al.*, Phys. Rev. Lett. **94**, 232501 (2005).
[13] C. Dossat *et al.*, Phys. Rev. C **72**, 054315 (2005).
[14] B. A. Brown and F. C. Barker, Phys. Rev. C **67**, 041304 (2003).
[15] L. Grigorenko *et al.*, Phys. Rev. C **64**, 054002 (2001).
[16] J. Rotureau, J. Okolowicz, and M. Ploszajczak, Nucl. Phys. **A767**, 13 (2006).
[17] R. Bellazzini *et al.*, Nucl. Instrum. Meth. **A424**, 444 (1999).
[18] IDE AS, www.ideas.no
[19] National Instruments, www.ni.com
[20] F. Sauli, Nucl. Instr. Meth. A **386**, 531 (1997).
[21] S. Bachmann *et al.*, Nucl. Instrum. Meth. **A438**, 376 (1999).
[22] S. Oda *et al.*, Nucl. Instr. Meth. **A566**, 312 (2006).
[23] A. Bressan *et al.*, Nucl. Instrum. Meth. **A425**, 254 (1999).
[24] J. Giovinazzo *et al.*, Phys. Rev. Lett. **99**, 102501 (2007).
[25] C. Dossat *et al.*, Nucl. Phys. A **792**, 18 (2007).
[26] K. Miernik *et al.*, Nucl. Instr. Meth. **A581**, 194 (2007).